Alma Mater Studiorum · Università di Bologna

**SCUOLA DI SCIENZE**
**Corso di Laurea in Fisica**

# Numerical Simulations of Anabatic Flow at different slope inclination

**Relatore:**
**Prof. Carlo Cintolesi**

**Presentata da:**
**Leonardo Fenech**

**Anno Accademico 2024/2025**

**Abstract**

Slope winds are thermally-driven atmospheric phenomena occurring over inclined terrains, playing a crucial role in local microclimates, pollutant dispersion, and wildfire propagation. Among these, anabatic (upslope) winds are generated by surface heating, which induces convective motions. While the foundational analytical model was established by Prandtl for laminar flows, real-world occurrences are inherently turbulent, necessitating advanced numerical tools for their accurate description.

This study employs Large-Eddy Simulation (LES) to investigate the turbulent structure of anabatic flows developing over an infinite, uniformly heated slope. The primary objective is to elucidate how the slope inclination angle influences the flow dynamics and transport mechanisms. The numerical simulations were conducted using a modified version of the `buoyantBoussinesqPimpleFoam` solver in OpenFOAM 6, incorporating a rotated coordinate system and specific adjustments to handle pressure boundary conditions on an infinite domain. Three different slope angles were examined: 15°, 30°, and 45°.

The results for the 30° case were successfully validated against benchmark Direct Numerical Simulation (DNS) data, confirming the accuracy of the LES setup in capturing the mean flow and turbulent statistics. The analysis of instantaneous fields revealed the presence of coherent structures, such as thermal plumes and longitudinal vortices, which are responsible for vertical heat and momentum transport. The comparative analysis across slope angles suggests that the observed flow characteristics may be influenced by multiple factors. Several possibilities could explain the results, including the specific choice of subgrid-scale modeling approach, the selected computational parameters, and the statistical convergence criteria employed. These findings highlight the complexity of numerically simulating stratified flows over sloping terrain and indicate the need for further investigation to fully isolate the role of topographic inclination on anabatic flow dynamics.

# Contents

# Introduction

Slope winds are fluid phenomena that occur in the presence of inclined topographic surfaces, such as hills or mountain slopes. In particular, thermally-driven slope winds are divided into two categories: katabatic (*katábasis*, "descending") and anabatic (*anábasis*, "ascending"). The study of these flows is particularly important for regions isolated from synoptic-scale phenomena: in these areas, such winds are crucial for characterizing local microclimates.

The effects of thermally driven winds can be highly varied. For example, they are important for pollen dispersal [Alba et al., 2000] and pollutant dispersion [Sabatier et al., 2020], for $CO_2$ transport in forested areas [Feigenwinter et al., 2010], and even for the migration of certain insect species [Drake and Farrow, 1988]. They also play a role in wildfire development, either spreading flames or confining fires to certain elevations [Sharples, 2009], and contribute to climatic processes by affecting Antarctic ice variability [Mezgec et al., 2017].

Katabatic winds are generated when surface air is colder than the surrounding air, causing the colder layer to descend along the slope, with warmer air occupying the vacated space. They form in shaded areas or during nighttime hours.

Anabatic winds are caused by higher boundary layer temperatures compared to air away from the surface at the same altitude, generating convective motion. The main difference between these two wind types lies in their stability: the former are generally associated with stable flows, while the latter are associated with turbulent motions due to the convective nature of the phenomenon [Whiteman, 2000].

The first analytical study was conducted by Prandtl [Prandtl et al., 2013], modeling one-dimensional laminar flows over uniformly heated or cooled inclined surfaces. The model solution is exact when using the Boussinesq approximation, revealing a linear relationship between downslope flow velocity, surface temperature difference, and heat flux. Although under certain conditions the model predictions are largely correct, some fundamental aspects of the phenomenon are neglected, particularly its turbulent nature.

To address this problem, various types of numerical simulations have been performed. Schumann [Schumann, 1990], building on Prandtl's work, conducted a LES (Large-Eddy Simulation) of a stratified fluid along an infinite, uniformly heated surface, paying attention to surface roughness. The emergence of coherent structures was observed, such as longitudinal vortices and Kelvin-Helmholtz waves, depending on the slope angle. Fedorovich and Shapiro [Fedorovich and Shapiro, 2009a] performed a DNS (Direct Numerical Simulation) of the same case, imposing a surface heat flux and studying Reynolds number dependence, observing how the mean flow behavior corresponds to that obtained by Prandtl. Subsequently, Giometto et al. [Giometto et al., 2017] studied the behavior at high Grashof numbers, again using DNS, focusing particularly on TKE (Turbulent Kinetic Energy) structure, identifying the division of the boundary layer into four distinct regions. More recently,

Xiao and Senocak [Xiao and Senocak, 2020] combined DNS with LSA (Linear Stability Analysis), introducing a new parameter called the stratification perturbation number, emphasizing perturbation growth and observing their persistence over time. Cintolesi et al. [Cintolesi et al., 2021], analyzing a double slope configuration using LES, detected thermal plumes and analyzed their role in vertical heat and momentum transport.

Experimentally, researchers have used various types of setups for studying the phenomenon. Reuten et al. [Reuten et al., 2007] used a sloped surface immersed in a water tank, comparing the results with data obtained by numerical models and field campaigns, observing agreement between them.

Princevac and Fernando [Princevac and Fernando, 2007], using a tank filled with a water-glycerin solution, studied how the slope angle and heat flux influenced the generation of turbulent flows, finding that the deflection of thermal plumes from the slope is inversely proportional to the Prandtl number and directly proportional to the slope angle, explaining the observations made by Hunt [Hunt et al., 2003]. Goldshmid and collaborators [Hilel Goldshmid et al., 2018], using a similar setup, studied how the presence of a plateau at the top of the slope influenced the flow, discovering a relation between the length of the slope, the width of the plateau, and the effective slope angle, a parameter used in this case to verify if the flow separated when reaching the apex.

For field observations, we recall the work of Whiteman et al.[Whiteman, 1982], who studied the atmospheric conditions of deep mountain valleys in Western Colorado via weather balloon, and the work done by Griffiths et al. [Griffiths et al., 2014], who observed the concentration of radon-222 hourly to detect the presence of anabatic winds at Jungfraujoch, a saddle in Switzerland.

The present study aims to investigate the influence of slope inclination on the turbulent dynamics and transport mechanisms of anabatic flows over uniformly heated infinite surfaces. Through Large-Eddy Simulation (LES) methodology implemented in OpenFOAM 6, we seek to elucidate how variations in slope angle ($\alpha = 15, 30, 45$) affect the fundamental characteristics of thermally-driven upslope flows.

# Chapter 1

# Computational Fluid Dynamics

## 1.1 Navier-Stokes Equations

### 1.1.1 Generalities

The motion of Newtonian fluids as a continuum is governed by the Navier-Stokes equations:

$$\rho \frac{Du_i}{Dt} = -\frac{\partial p}{\partial x_i} + \rho g_i + \frac{\partial}{\partial x_j}\left[2\mu e_{ij} - \frac{2}{3}\mu(\nabla \cdot \mathbf{u})\delta_{ij}\right], \tag{1.1}$$

where $\rho$ denotes the fluid density, $p$ the pressure, $\mathbf{u} = (u_i)$ the velocity field, $g_i$ the gravitational acceleration, $\mu$ the dynamic viscosity, $e_{ij} = \frac{1}{2}(\partial u_i/\partial x_j + \partial u_j/\partial x_i)$ the strain-rate tensor, while $\delta_{ij}$ is the Kronecker delta. In this equation appears the material derivative, representing the time rate of change following a fluid element, is defined as:

$$\frac{D}{Dt} = \frac{\partial}{\partial t} + u_j \frac{\partial}{\partial x_j} \tag{1.2}$$

In various cases, it's possible to consider the fluid incompressible, reducing Eq.1.1 to:

$$\begin{aligned} &\nabla \cdot \mathbf{u} = 0 \\ &\rho \frac{D\mathbf{u}}{Dt} = -\nabla p + \rho \mathbf{g} + \mu \nabla^2 \mathbf{u} \end{aligned} \tag{1.3}$$

In Eq.1.3 the first equation is the continuity equation for incompressible fluids and the second one the momentum equation. It's possible to rewrite Eq.1.3 in a non-dimensional form; to do so we need to select the appropriate scale for Eq.1.1 form a set of non-linear coupled partial differential equations. The non-linearity emerge from the convective term of the material derivative (Eq.1.2) and has various implications: from a pure physical standpoint, the most notable is the emergence of turbulence at high Reynolds numbers.

### 1.1.2 The Boussinesq approximation

For systems with incompressible fluids where relative density variations satisfy $\Delta\rho/\rho_0 \ll 1\%$, the Boussinesq approximation yields:

$$
\begin{aligned}
&\nabla \cdot \mathbf{u} = 0 \\
&\frac{Du_i}{Dt} = -\frac{\partial \Pi}{\partial x_i} + \frac{\rho - \rho_0}{\rho_0} g_i + \frac{\partial}{\partial x_j}(\nu \frac{\partial u_i}{\partial x_j}) \\
&\frac{DT}{Dt} = \frac{\partial}{\partial x_j}(\kappa \frac{\partial T}{\partial x_j}) \\
&\rho = \rho_0[1 - \alpha(T - T_0)]
\end{aligned}
\tag{1.4}
$$

where $\Pi$ denotes the kinematic pressure deviation, $\nu$ the kinematic viscosity, $\kappa$ the thermal diffusivity, $\alpha$ the thermal expansion coefficient and $\rho_0, T_0$ the reference density and temperature. The Boussinesq approximation applies if the temperature differences in the fluid are small and the vertical scale of the flow is not too large. Eq.1.4 are composed of the continuity equation for incompressible fluids, the momentum equation, the heat equation and the equation of state.

## 1.2 Turbulence

### 1.2.1 Characteristics of turbulent flows

Turbulent flows, unlike laminar flows, are chaotic, nonlinear and highly sensitive to initial conditions [Kundu et al., 2012]. Such flows must exhibit the following characteristics:

- **Randomness**: Fluctuations in flow quantities (e.g., velocity, pressure) are stochastic and irregular.
- **Nonlinearity**: Small perturbations grow exponentially due to nonlinear interactions, governed primarily by the Reynolds number ($Re$), which quantifies the ratio of inertial to viscous forces.
- **Diffusivity**: Turbulent flows exhibit enhanced transport of momentum, heat, and mass compared to laminar flows.
- **Vorticity**: The flow contains coherent, rotating structures called *eddies* with a broad range of scales. The largest eddies dominate the kinetic energy, while smaller eddies contribute to energy cascading.
- **Dissipation**: Energy is transferred from larger to smaller eddies through vortex stretching until viscous effects dissipate it into heat (Kolmogorov's dissipation scale).

### 1.2.2 Energy cascade and Kolmogorov Hypotheses

Turbulent flows are fundamentally characterized by the *energy cascade* process: energy enters the system through the largest eddies, is transferred to progressively smaller scales, and is ultimately dissipated by viscous effects at the smallest scales. To quantify this phenomenon, we define the following quantities: $l$ the characteristic size of an eddy, $u(l)$ the characteristic velocity scale of an eddy of size $l$, $\tau(l) = l/u(l)$ the turnover (or dynamical) timescale of an eddy and $l_0$ the integral scale (size of the largest energy-containing eddies). Andrey Kolmogorov in 1941 created a theory that rests on two key hypotheses:

1. **Local isotropy**: At sufficiently small scales ($l \ll l_0$), turbulence becomes statistically isotropic (direction-independent).

2. **Universality**: In the *inertial subrange* (scales smaller than $l_0$ but larger than the dissipation scale $\eta$), the energy spectrum depends only on the energy dissipation rate per unit mass $\varepsilon$ and the wavenumber $k \sim 1/l$.

While we won't examine the reasoning behind these hypotheses, their consequences are profound. The Kolmogorov microscales emerge from dimensional analysis of the dissipative range, defined by the following fundamental relations:

$$\eta = \left(\frac{\nu^3}{\varepsilon}\right)^{1/4} \tag{1.5}$$

$$u_\eta = (\nu\varepsilon)^{1/4} \tag{1.6}$$

$$\tau_\eta = \left(\frac{\nu}{\varepsilon}\right)^{1/2} \tag{1.7}$$

where: $\eta$ is the Kolmogorov length scale $u_\eta$ is the Kolmogorov velocity scale $\tau_\eta$ is the Kolmogorov time scale $\nu$ is the kinematic viscosity $\varepsilon$ is the energy dissipation rate per unit mass
These scales describe the regime where viscous forces finally overcome inertial motions, converting kinetic energy into heat. The length scale $\eta$ represents the physical size below which turbulent eddies cannot persist - it marks the ultimate limit of the energy cascade where all remaining motion becomes smooth and laminar. The corresponding velocity scale $u_\eta$ indicates how fast these smallest eddies rotate before being annihilated by viscosity, while $\tau_\eta$ gives their characteristic lifetime before energy is completely dissipated.

### 1.2.3 Energy Spectrum and Turbulent Kinetic Energy

The turbulent kinetic energy (TKE), denoted $k$, represents the mean kinetic energy per unit mass contained in velocity fluctuations and serves as a fundamental measure of turbulence intensity. This quantity is defined as:

$$k = \frac{1}{2}\overline{u_i' u_i'} = \frac{1}{2}(\overline{u'^2} + \overline{v'^2} + \overline{w'^2}) \tag{1.8}$$

where: $k$ is the turbulent kinetic energy $\bar{\cdot}$ indicates Reynolds (temporal) averaging $u_i'$ are velocity fluctuations relative to the mean flow ($u_i' = u_i - \overline{u_i}$)
The energy distribution across scales is described by the spectrum $E(k_w)$, which relates to TKE through:

$$k = \int_0^\infty E(k_w)\, dk_w \tag{1.9}$$

where $E(k_w)$ is the energy spectrum as a function of wavenumber and $k_w$ is the wavenumber ($k_w \sim 1/l$).
The dissipation rate $\varepsilon$, governing energy conversion to heat, is determined by the fluctuating strain rate:

$$\varepsilon = 2\nu\overline{S_{ij}' S_{ij}'}, \quad S_{ij}' = \frac{1}{2}\left(\frac{\partial u_i'}{\partial x_j} + \frac{\partial u_j'}{\partial x_i}\right) \tag{1.10}$$

where: $S'_{ij}$ is the fluctuating strain rate tensor.
In the inertial subrange ($1/l_0 \ll k_w \ll 1/\eta$), Kolmogorov's theory predicts the universal scaling:

$$E(k_w) = \alpha_k \varepsilon^{2/3} k_w^{-5/3} \tag{1.11}$$

where $\alpha_k \approx 1.5$ is the Kolmogorov constant.
The $-5/3$ exponent reflects the constant energy flux through the cascade. The spectrum transitions from energy-containing scales ($k_w \sim 1/l_0$) through the inertial range to the dissipation range ($k_w > 1/\eta$), where viscous effects dominate.

## 1.3 Large-Eddy Simulation

Large-Eddy Simulation represents a computationally efficient approach to modeling turbulent flows by exploiting the inherent scale separation in turbulence. This methodology addresses the fundamental challenge of turbulence modeling: the prohibitive computational cost of resolving all scales of motion while maintaining sufficient accuracy for practical applications. The theoretical foundation of LES rests on Kolmogorov's energy cascade theory, which demonstrates that large-scale eddies contain most of the turbulent kinetic energy and exhibit strong dependence on boundary conditions and geometry, while smaller scales display more universal characteristics.

### 1.3.1 Theoretical Foundation and Filtering Operation

The motivation for LES emerges from the computational scaling properties of turbulent flows. Direct Numerical Simulation requires resolution of all turbulent scales from the energy-containing eddies down to the Kolmogorov microscale $\eta$, resulting in computational requirements that scale as $Re^{9/4}$ for high Reynolds number flows. This scaling renders DNS impractical for most engineering applications involving complex geometries or atmospheric flows.
LES circumvents this limitation by recognizing that large eddies ($l > \Delta$, where $\Delta$ is the filter width) carry most of the turbulent kinetic energy and Reynolds stresses while being highly dependent on flow-specific boundary conditions. Conversely, small eddies ($l < \Delta$) in the inertial and dissipative ranges exhibit universal behavior described by Kolmogorov's $k_w^{-5/3}$ spectrum. This scale separation justifies resolving only the large, energetic scales while modeling the universal small-scale motions through subgrid-scale (SGS) models.
The filtering operation that defines LES can be expressed mathematically for any field variable $\phi$ as:

$$\bar{\phi}(x,t) = \int_\Omega G(r,x)\phi(x-r,t)dr \tag{1.12}$$

where $\bar{\phi}(x,t)$ represents the spatially filtered field, $G(r,x)$ is the filter kernel satisfying $\int_\Omega G(r,x)dr = 1$, and $\Omega$ is the integration domain. The decomposition of the instantaneous field follows:

$$\phi(x,t) = \bar{\phi}(x,t) + \phi''(x,t) \tag{1.13}$$

where $\phi''(x,t)$ denotes the subgrid-scale component, fundamentally distinct from the temporal fluctuations $\phi'$ in Reynolds-averaged approaches.

Applying the spatial filtering operation to the incompressible Navier-Stokes equations yields the filtered momentum and continuity equations:

$$\frac{\partial \overline{u}_j}{\partial x_j} = 0 \tag{1.14}$$

$$\frac{\partial \overline{u}_i}{\partial t} + \frac{\partial \overline{u}_j \overline{u}_i}{\partial x_j} = -\frac{\partial \overline{p}}{\partial x_i} + \frac{\partial}{\partial x_j}\left[\nu \frac{\partial \overline{u}_i}{\partial x_j}\right] - \frac{\partial \tau_{ij}^r}{\partial x_j} \tag{1.15}$$

The central challenge in LES lies in modeling the residual stress tensor $\tau_{ij}^r = \overline{u_i u_j} - \bar{u}_i \bar{u}_j$, which represents the influence of unresolved subgrid scales on the resolved motion. This tensor cannot be computed directly from the resolved fields and requires closure modeling. The turbulent kinetic energy in LES naturally decomposes into resolved and subgrid-scale components:

$$k_{total} = k_{resolved} + k_{sgs} = \frac{1}{2}\overline{u_i' u_i'} + \frac{1}{2}\overline{u_i'' u_i''} \tag{1.16}$$

This decomposition emphasizes the physical interpretation of LES filtering: the resolved field $\overline{\phi}$ represents the component observable by a hypothetical detector of size $\Delta$, while the subgrid component accounts for all unresolved motions smaller than the filter scale.

### 1.3.2 The Smagorinsky Model and Scalar Transport

The most widely employed closure for the residual stress tensor is the Smagorinsky model, which applies the eddy viscosity hypothesis:

$$\tau_{ij}^r = -2\nu_t \bar{S}_{ij} + \frac{1}{3}\tau_{kk}^r \delta_{ij} \tag{1.17}$$

where the resolved strain rate tensor $\overline{S}_{ij} = \frac{1}{2}\left(\frac{\partial \overline{u}_i}{\partial x_j} + \frac{\partial \overline{u}_j}{\partial x_i}\right)$ characterizes the deformation of the resolved flow field. The isotropic component $\frac{1}{3}\tau_{kk}^r \delta_{ij}$ is typically absorbed into a modified pressure term.
The subgrid-scale viscosity follows the mixing-length formulation:

$$\nu_t = (C_S \Delta)^2 |\overline{S}| \tag{1.18}$$

where $C_S \approx 0.17$ is the Smagorinsky coefficient, $\Delta$ represents the filter width (typically related to grid spacing as $\Delta = (\Delta x \Delta y \Delta z)^{1/3}$), and $|\bar{S}| = \sqrt{2\bar{S}_{ij}\bar{S}_{ij}}$ measures the magnitude of the resolved strain rate.
The physical interpretation of this model assumes that the most energetic unresolved eddies have characteristic length scale $l_s = C_S \Delta$ and participate in local equilibrium between production and dissipation of subgrid-scale energy. The energy transfer rate from resolved to subgrid scales is:

$$P_{sgs} = 2\nu_t |\bar{S}|^2 = 2(C_S \Delta)^2 |\bar{S}|^3 \geq 0 \tag{1.19}$$

This formulation ensures that the model is purely dissipative, always extracting energy from the resolved scales. While this behavior is generally correct for the forward energy cascade, it cannot represent the physically important phenomenon of energy backscatter from small to large scales that occurs intermittently in real turbulent flows.

Near solid boundaries, the model requires modification to account for the damping effects of viscous forces. The Van Driest damping function provides this correction:

$$l_s = C_S \Delta \left[ 1 - \exp\left( -\frac{y^+}{A^+} \right) \right] \tag{1.20}$$

where $y^+ = y u_\tau / \nu$ represents the dimensionless wall distance in wall units, $u_\tau$ is the friction velocity, and $A^+ \approx 25$ is an empirical constant. This formulation ensures that the SGS viscosity approaches zero at the wall, where viscous effects dominate turbulent motions.

The extension of LES to scalar transport follows the same filtering principles applied to momentum equations. For a passive scalar $\theta$, the filtered transport equation becomes:

$$\frac{\partial \overline{\theta}}{\partial t} + \frac{\partial \overline{u}_j \overline{\theta}}{\partial x_j} = \frac{\partial}{\partial x_j} \left[ \kappa \frac{\partial \overline{\theta}}{\partial x_j} \right] - \frac{\partial q_j}{\partial x_j} + S_\theta \tag{1.21}$$

where $q_j = \overline{u_j \theta} - \overline{u}_j \overline{\theta}$ represents the subgrid-scale scalar flux requiring closure modeling. The gradient-diffusion hypothesis provides the most common closure:

$$q_j = -\kappa_t \frac{\partial \overline{\theta}}{\partial x_j} \tag{1.22}$$

where the turbulent scalar diffusivity $\kappa_t = \nu_t / Pr_t$ relates to the SGS viscosity through the turbulent Prandtl number $Pr_t \approx 0.9$. This relationship assumes that momentum and scalar transport exhibit similar behavior in the subgrid scales, an approximation that proves adequate for most atmospheric applications including anabatic flow simulations.

### 1.3.3 Implementation Considerations and Model Limitations

The practical implementation of LES depends critically on the relationship between the computational grid and the implicit filtering operation. In most applications, the filter width is implicitly defined by the grid spacing, with $\Delta = (\Delta x \Delta y \Delta z)^{1/3}$ providing a representative measure. This implicit filtering means that the numerical discretization scheme directly influences the effective filter characteristics.

High-order numerical schemes with minimal numerical dissipation provide sharp spectral cutoffs that approximate the ideal LES filter. Conversely, lower-order schemes introduce numerical dissipation that can overwhelm the subgrid-scale model, leading to excessive damping of turbulent fluctuations. The choice of discretization scheme therefore represents a crucial consideration in LES implementation.

Grid anisotropy presents another significant challenge in LES applications. When the grid stretching ratio exceeds approximately 3:1, the assumption that $\Delta$ represents a characteristic length scale in all coordinate directions becomes questionable. This anisotropy can introduce artificial directional bias in the subgrid stresses, potentially degrading the simulation accuracy. For anabatic flow simulations, where near-wall resolution requirements often necessitate significant grid stretching in the wall-normal direction, careful attention to these grid effects becomes essential for maintaining simulation fidelity.

The standard Smagorinsky model exhibits several well-documented limitations that become particularly relevant in the context of stratified flows like anabatic circulation. Its purely dissipative nature prevents representation of energy backscatter, while its

dependence on the local strain rate leads to insufficient SGS viscosity in regions with weak velocity gradients, such as flow separation zones or the core regions of large eddies where active subgrid-scale turbulence may still exist.

# Chapter 2

# Large-Eddy Simulation of anabatic flow at different inclination

## 2.1 Problem Definition

### 2.1.1 Governing equations

To simulate anabatic flows effectively, we adopt a rotated reference frame, following the methodologies of [Schumann, 1990], [Fedorovich and Shapiro, 2009b], and [Giometto et al., 2017]. The coordinate system $(\hat{x}, \hat{y}, \hat{z})$ is derived by rotating a conventional Cartesian frame $(\hat{x}', \hat{y}', \hat{z}')$ by an angle $\alpha$ about the $\hat{y}'$-axis. In this way, we will have the gravitational acceleration opposite to the $\hat{z}'$-axis, with $\hat{z}$-axis normal to the inclined plane, $\hat{x}$ alongside the stream-wise direction and $\hat{y}$ alongside the span-wise direction. The potential temperature $\theta$ is decomposed into the background profile $\theta^R$ and its fluctuations $\theta''$ (following [Prandtl et al., 2013] and [Giometto et al., 2017]), allowing the Brunt-Väisälä frequency to be defined as:

$$N \equiv \sqrt{\beta \frac{d\theta^R}{dz'}}, \tag{2.1}$$

where $\beta \equiv g/\theta_0$ is the buoyancy parameter, with $g$ denoting the gravitational acceleration magnitude and $\theta_0$ a reference constant temperature. Considering air and temperature variations of $15K$, is possible to adopt the Boussinesq approximation, having errors less than 1% ([Kundu et al., 2012]). The set of Eq.1.4 in our coordinate system and using the new notations becomes:

$$\frac{\partial u_j}{\partial x_j} = 0 \tag{2.2}$$

$$\frac{\partial u_i}{\partial t} + \frac{\partial u_j u_i}{\partial x_j} = -k_i \beta \theta'' - \frac{\partial \Pi}{\partial x_i} + \frac{\partial}{\partial x_j}\left(\nu \frac{\partial u_i}{\partial x_j}\right) \tag{2.3}$$

$$\frac{\partial \theta''}{\partial t} + \frac{\partial u_j \theta''}{\partial x_j} = -\frac{\partial u_j \theta^R}{\partial x_j} + \frac{\partial}{\partial x_j}\left(\kappa \frac{\partial \theta''}{\partial x_j}\right) \tag{2.4}$$

where $k_i = -(sin(\alpha), 0, \cos(\alpha))$ is the gravity unity vector and $\Pi = (P - \rho_0 g_i x_i)/\rho_0$ is the deviation from the kinematic hydrostatic pressure.
Eq.2.2, 2.3, 2.4 can be rewritten using the buoyancy $b \equiv \beta\theta''$ and considering that $\theta^R$

only depends on $z'$, obtaining:

$$\begin{aligned}
&\frac{\partial u_j}{\partial x_j} = 0 \\
&\frac{\partial u_i}{\partial t} + \frac{\partial u_j u_i}{\partial x_j} = -k_i b - \frac{\partial \Pi}{\partial x_i} + \frac{\partial}{\partial x_j}\left(\nu \frac{\partial u_i}{\partial x_j}\right) \\
&\frac{\partial b}{\partial t} + \frac{\partial u_j b}{\partial x_j} = N^2 u_j k_j + \frac{\partial}{\partial x_j}\left(\kappa \frac{\partial b}{\partial x_j}\right)
\end{aligned} \tag{2.5}$$

Following [Giometto et al., 2017], it is convenient to introduce a set of characteristic parameters to normalize the governing equations. The normalization is based on the surface buoyancy $b_S > 0$ and the Brunt-Väisälä frequency $N$, defining the following characteristic scales:

$$\begin{aligned}
&T \equiv N^{-1}, \quad L \equiv \tfrac{|b_S|}{N^2}, \\
&B \equiv |b_S|, \quad U \equiv \tfrac{|b_S|}{N}
\end{aligned} \tag{2.6}$$

Using these scales, the following dimensionless variables are introduced:

$$\begin{aligned}
&t^* \equiv \tfrac{t}{T}, \quad x_i^* \equiv \tfrac{x_i}{L}, \quad b^* \equiv \tfrac{b}{B}, \\
&u_i^* \equiv \tfrac{u_i}{U}, \quad \Pi^* \equiv \tfrac{\Pi}{U^2}
\end{aligned} \tag{2.7}$$

Substituting these dimensionless variables into the governing Equations 2.5, we obtain the dimensionless form:

$$\begin{aligned}
&\frac{\partial u_j^*}{\partial x_j^*} = 0 \\
&\frac{\partial u_i^*}{\partial t^*} + \frac{\partial u_j^* u_i^*}{\partial x_j^*} = -k_i b^* - \frac{\partial \Pi^*}{\partial x_i^*} + Gr^{-1/2} \frac{\partial}{\partial x_j^*}\left(\frac{\partial u_i^*}{\partial x_j^*}\right) \\
&\frac{\partial b^*}{\partial t^*} + \frac{\partial u_j^* b^*}{\partial x_j^*} = u_j^* k_j + (Gr^{-1/2} Pr^{-1}) \frac{\partial}{\partial x_j^*}\left(\frac{\partial b^*}{\partial x_j^*}\right)
\end{aligned} \tag{2.8}$$

where two important dimensionless numbers appear:
- The *Prandtl number*: $Pr = \nu/\kappa$, representing the ratio between the hydrodynamic boundary layer and the thermal boundary layer thickness.
- The *Grashof number*: $Gr \equiv b_S^4/\nu^2 N^6$, representing the ratio between buoyancy forces and viscous forces.

The Grashof number is particularly significant in anabatic flows as it characterizes the relative importance of buoyancy-driven convection compared to molecular diffusion. Large values of $Gr$ indicate that buoyancy forces dominate over viscous effects, leading to more vigorous convective motions along the slope.

For the analysis of turbulent processes in anabatic flows, it is useful to derive the conservation equation for the dimensionless turbulent kinetic energy $k'^* \equiv k'/U^2$, where $k' = \frac{1}{2}\langle u_i' u_i' \rangle$ and $u_i' = u_i - \langle u_i \rangle$ represents the velocity fluctuations. Following the derivation in [Giometto et al., 2017], the dimensionless TKE equation reads:

$$\begin{aligned}
\frac{\partial k'^*}{\partial t^*} = &-\langle b'^* u_j'^* \rangle k_j - \frac{\partial \langle \Pi'^* u_z'^* \rangle}{\partial z^*} - \langle u_x'^* u_z'^* \rangle \frac{\partial \langle u_x^* \rangle}{\partial z^*} \\
&- \frac{\partial}{\partial z^*}\left(\frac{1}{2}\langle u_i'^* u_i'^* u_z'^* \rangle\right) + Gr^{-1/2} \frac{\partial^2 k'^*}{\partial z^{*2}} - Gr^{-1/2} \left\langle \frac{\partial u_i'^*}{\partial x_j^*} \frac{\partial u_i'^*}{\partial x_j^*} \right\rangle
\end{aligned} \tag{2.9}$$

## 2.2 Numerical Setup

### 2.2.1 Geometry and computational mesh

The computational mesh employed for the simulation is orthogonal, static, and structured, with a grid resolution of $96 \times 96 \times 256$ cells in the three coordinate directions. Following the configuration adopted by [Giometto et al., 2017], the computational domain spans normalized dimensions of $[0, 0.0241] \times [0, 0.0241] \times [0, 0.0324]$. For clarity, we identify the slope surface as the floor and the opposing boundary as the ceiling. To better resolve near-surface phenomena, the mesh incorporates hyperbolic stretching along the $\hat{z}$-direction, providing enhanced refinement near the floor boundary.

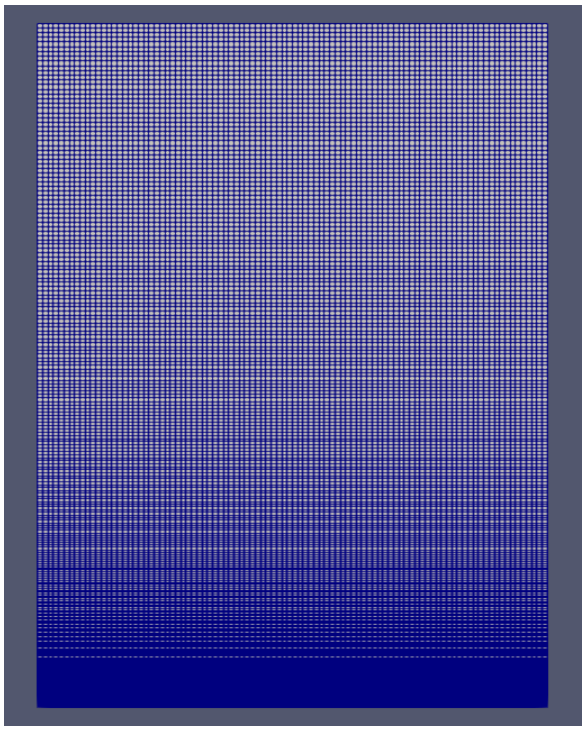

Figure 2.1: Computational mesh structure

### 2.2.2 Parameters

The case was simulated for three distinct slope inclination angles $\alpha$: 15°, 30°, and 45°. These configurations will be referred to as $\alpha_{15}$, $\alpha_{30}$, and $\alpha_{45}$, respectively. All simulations employed identical physical parameters, as documented in Table 2.1.

| $\nu\,(m^2/s)$ | $b_s\,(m/s^2)$ | $N\,(s^{-1})$ | $Gr$ |
|---|---|---|---|
| $1.5 \times 10^{-5}$ | 1 | 0.526 | $2.1 \times 10^{11}$ |

Table 2.1: Physical parameters used in the simulation

The simulation duration was determined based on the characteristic period of internal gravity waves, defined as $T_p = 2\pi / \sin(\alpha)$ ([McNider, 1982]). Following the methodology of [Giometto et al., 2017], the total simulation time was set to exceed $6T_p$ to ensure complete flow development and statistical stationarity. For consistency across all cases, a fixed duration of 288 seconds was adopted.

### 2.2.3 Initial and boundary conditions

The fluid is initially at rest, with all internal field variables set to zero as the initial condition. The boundary conditions applied to the system are summarized in Table 2.2.

| Face | $\overline{u}_i$ | $\overline{b}$ | $\overline{\Pi}$ | $\overline{\nu}_t$ | $\overline{\kappa}_t$ |
|---|---|---|---|---|---|
| Floor | $\overline{u}_i = 0$ | $\overline{b} = b_S$ | zero-gradient | zero-gradient | zero-gradient |
| Ceiling | zero-gradient | $\overline{b} = 0$ | $\overline{\Pi} = 0$ | zero-gradient | zero-gradient |
| Vertical faces | cyclic | cyclic | cyclic | cyclic | cyclic |

Table 2.2: Boundary conditions

The physical interpretation of the applied boundary conditions is as follows:

- **Floor Boundary**
  - $\bar{u}_i = 0$: *No-slip condition*
    The fluid velocity is zero at the floor.
  - $\bar{b} = b_S$: *Fixed buoyancy*
    Maintains constant density difference at the boundary, representing a heat source.
  - *Zero-gradient* for $\bar{\Pi}$, $\bar{\nu}_i$, $\bar{\kappa}_i$:
    No transport through the wall.
- **Ceiling Boundary**
  - $\bar{b} = 0$: *Neutral buoyancy*
    Sets reference density state.
  - $\bar{\Pi} = 0$: *Reference pressure*
    Fixes pressure baseline to prevent numerical drift.
  - *Zero-gradient* for $\bar{u}_i$: *Free-slip*
    Allows fluid to move parallel to the surface without friction.
- **Vertical Boundaries**
  - *Cyclic conditions*:
    Connects opposite boundaries to simulate infinite horizontal extent, eliminating edge effects.

### 2.2.4 Solver Modifications and Numerical Schemes

The simulation was conducted using a modified version of OpenFOAM's `buoyantBoussinesqPimpleFoam` solver, adapted specifically for anabatic flows. The key modifications were necessary to handle the physics of stratified flows on an inclined plane while ensuring compatibility with cyclic boundary conditions that simulate an infinite slope.

### Main Solver Structure

The modified solver follows the PIMPLE algorithm, which combines the SIMPLE and PISO methods for pressure-velocity coupling in transient flows. This approach allows for larger time steps while maintaining numerical stability, which is essential for LES simulations where computational efficiency is crucial.
The solution procedure consists of a time loop with nested correction loops:

```
while (pimple.loop())
{
    #include "UEqn.H"      // Momentum equation
    #include "bEqn.H"      // Buoyancy equation

    while (pimple.correct())
    {
        #include "pEqn.H"  // Pressure correction
    }

    if (pimple.turbCorr())
    {
        turbulence->correct();  // Update SGS model
    }
}
```

Listing 2.1: Main time-stepping loop structure.

This structure ensures proper coupling between momentum, buoyancy, and pressure fields. The outer loop handles the predictor steps for velocity and scalar transport, while the inner loop corrects the pressure field to satisfy continuity. The turbulence model is updated according to the Smagorinsky formulation.

### Critical Modification: Pressure Treatment for Cyclic Boundaries

The most important modification addressed a fundamental issue with the original solver's pressure formulation. The standard approach included position-dependent hydrostatic terms that violated the periodicity required for cyclic boundary conditions on an infinite inclined plane.
The solution involved redefining the pressure variable to match our theoretical framework:

$$\texttt{p\_rgh} = \frac{P - \rho_0 g_i x_i}{\rho_0} = \overline{\Pi} \tag{2.10}$$

This removes the hydrostatic pressure component, preserving only the dynamic pressure deviations that can properly satisfy periodic boundary conditions. For infinite domains with cyclic boundaries, the hydrostatic component must be treated as an explicit body force rather than a pressure gradient to maintain mathematical consistency.
The modification required removing the hydrostatic term `phig` from the pressure equation:

```
// Remove the hydrostatic contribution for cyclic boundaries
// surfaceScalarField phig(-rAUf*khf*fvc::snGrad(rhok)*mesh.magSf())
    ;

surfaceScalarField phiHbyA
(
    "phiHbyA",
```

```
    fvc::flux(HbyA)
  + MRF.zeroFilter(rAUf*fvc::ddtCorr(U, phi))
//  + phig  // This term is removed for cyclic compatibility
);
```

Listing 2.2: Removal of hydrostatic contribution in pressure equation.

### Momentum Equation with Buoyancy Forcing

To compensate for removing the hydrostatic pressure gradient, the buoyancy force term $-\bar{b}\mathbf{k}$ was added explicitly to the momentum equation. This ensures gravitational effects are correctly represented while maintaining cyclic compatibility:

```
fvVectorMatrix UEqn
(
    fvm::ddt(U)
  + fvm::div(phi, U)
  + turbulence->divDevReff(U)
 ==
    - b*k                       // Explicit buoyancy forcing
  + fvOptions(U)
);
```

Listing 2.3: Explicit buoyancy forcing in momentum equation.

Here, the gravity vector $\mathbf{k} = (-\sin(\alpha), 0, \cos(\alpha))$ accounts for the inclined coordinate system, directly implementing the term $-k_i\bar{b}$ from the filtered momentum equation.

### Buoyancy Transport with Stratification Effects

The buoyancy equation required significant modification to include the background stratification source term $N^2\overline{u}_j k_j$. This term represents the crucial interaction between the flow and the ambient atmospheric stability, arising from the advection of the background potential temperature profile.

```
{
    alphat = turbulence->nut()/Prt;
    volScalarField alphaEff("alphaEff", turbulence->nu()/Pr + alphat
        );
    volScalarField source("source", N2*(U & k));

    fvScalarMatrix bEqn
    (
        fvm::ddt(b)
      + fvm::div(phi, b)
      - fvm::laplacian(alphaEff, b)
     ==
        fvm::Sp(0.25*source, b)       // Implicit contribution
      + source*(1.0 - 0.25*b)        // Explicit contribution
      + fvOptions(b)
    );

    bEqn.solve();
}
```

Listing 2.4: Buoyancy equation with stratification source.

The effective thermal diffusivity `alphaEff` combines molecular ($\nu/Pr$) and turbulent ($\nu_t/Pr_t$) contributions, where $Pr_t = 0.9$. The mixed implicit-explicit treatment of the

stratification source term (75% explicit, 25% implicit) enhances numerical stability by improving the diagonal dominance of the coefficient matrix while avoiding potential instabilities from fully explicit treatment.

### Numerical Discretization

Second-order accuracy was maintained throughout the simulation using carefully selected discretization schemes:

**Temporal Schemes:**

- **Time derivatives**: Second-order backward Euler (SOUE) for all transient terms
- This provides good stability properties while maintaining temporal accuracy for LES applications

**Spatial Schemes:**

- **Gradients and Laplacians**: Gaussian integration with linear interpolation
- **Advection terms**:
  - Bounded Gamma scheme for momentum transport to prevent oscillations
  - MUSCL scheme for buoyancy transport to ensure monotonicity

The Gamma scheme automatically switches between second-order central differencing in smooth regions and first-order upwinding near sharp gradients, making it well-suited for turbulent flows. The MUSCL scheme provides similar adaptive behavior for scalar transport while keeping the buoyancy field physically bounded.

**Sub-Grid Scale Model Implementation:** The Smagorinsky model implementation follows the formulation described in Section **??**, with near-wall damping applied using:

$$\nu_t = (C_s\Delta)^2|\overline{\mathbf{S}}|\left[1-\exp\left(-\frac{y^+}{A^+}\right)\right]^2 \tag{2.11}$$

where the squared damping function provides more accurate representation of the viscous-turbulent transition compared to the linear form.

**Linear System Solution:** The discretized equations are solved using efficient algebraic methods:

- **Pressure correction**: GAMG (Generalized Algebraic Multi-Grid) solver with geometric-algebraic coarsening
- **Momentum and scalar equations**: BiCGStab with diagonal incomplete-LU preconditioning

The structured orthogonal mesh eliminates the need for non-orthogonal corrections, simplifying the numerical setup and improving computational efficiency. The mesh quality ensures that surface-normal vectors align with coordinate directions, avoiding iterative corrections required for skewed cells.

## 2.3 Results

This section presents the analysis of the simulation results, beginning with a rigorous validation against the benchmark DNS data from [Giometto et al., 2017] for the $\alpha_{30}$ slope case. This is followed by a comparative investigation of the flow characteristics across the three different slope angles. All profiles are presented with the normalized height $z/L$ on the ordinate axis, where $L$ denotes the characteristic length scale of the flow domain. This normalization allows for a consistent comparison across different flow configurations and facilitates the identification of scaling relationships in the turbulent boundary layer development. The validation serves to establish the credibility of the present numerical setup and methodology, while the subsequent parametric analysis aims to elucidate the sensitivity of anabatic flow dynamics to variations in slope inclination.

### 2.3.1 Validation against DNS Benchmark Data

The numerical results for the $\alpha_{30}$ case were quantitatively compared against the benchmark DNS data from [Giometto et al., 2017]. Figure 2.2 shows the comparison

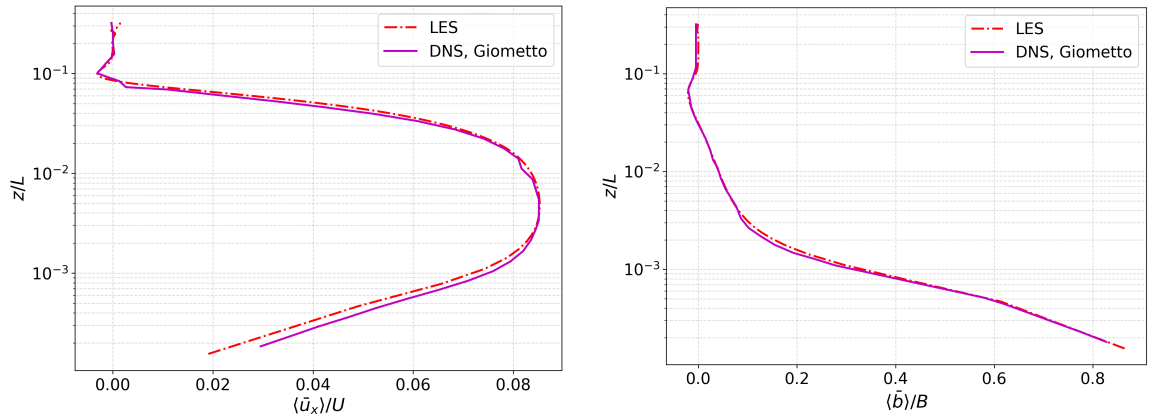


(a) Vertical profile of normalized mean streamwise velocity.

(b) Vertical profile of normalized mean buoyancy.

Figure 2.2: Comparison of mean profiles from the present $\alpha_{30}$ and the reference DNS data.

of the first-order statistics. The mean streamwise velocity profile (Fig.2.2a) exhibits excellent agreement with the DNS benchmark. The present LES accurately captures the key features: the near-wall velocity increase, the magnitude and position of the velocity maximum at $z/L \approx 6 \times 10^{-3}$, and the subsequent decay towards zero in the outer layer, including the faint back-flow region around $z/L \approx 0.1$. The normalized mean buoyancy profile $\langle \bar{b} \rangle / B$ (Fig.2.2b) also shows very good agreement. The simulation correctly replicates the strong positive buoyancy at the wall ($\langle \bar{b} \rangle / B = 1$), the steep gradient in the immediate vicinity of the surface ($z/L < 3 \times 10^{-3}$), and the subsequent gradual decrease with height. The comparison of the second-order statistics, shown in Figures 2.3 and 2.4, demonstrates the capability of the present LES to capture the turbulent structure of the flow. The vertical distribution and magnitude of the velocity fluctuations are well reproduced. The RMS of the streamwise velocity component (Fig.2.3a) is slightly under-predicted in the region of its peak value ($2 \times 10^{-3} < z/L < 8 \times 10^{-2}$). The spanwise velocity fluctuations (Fig.2.4a) are ac-

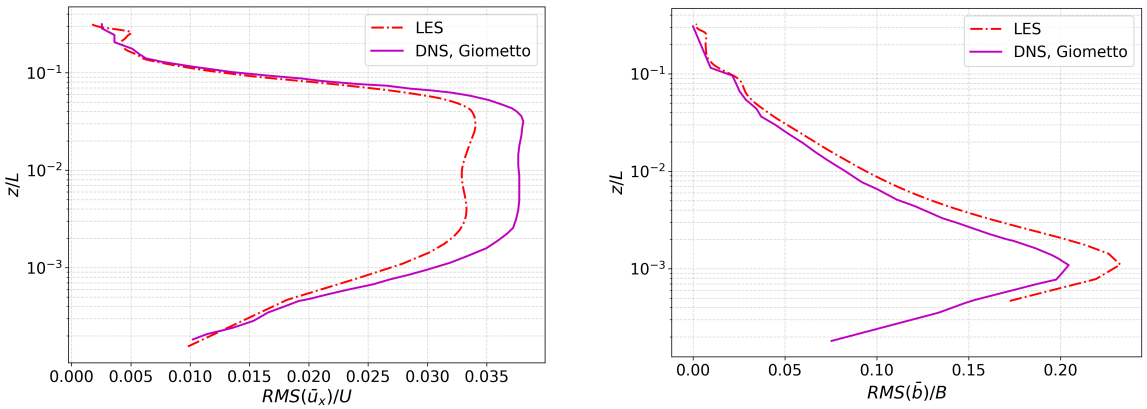


(a) Streamwise velocity fluctuations

(b) Buoyancy fluctuations

Figure 2.3: Comparison of RMS values of $\overline{u}_x$ and $\overline{b}$ from the present $\alpha_{30}$ and the reference DNS data.

curately captured across the entire domain height. The vertical velocity fluctuations (Fig.2.4b) show good agreement in the outer region but are slightly under-predicted in the near-wall region ($z/L < 5 \times 10^{-2}$). The buoyancy fluctuations (Fig.2.3b) are accurately captured in the outer layer, including the pronounced maximum.

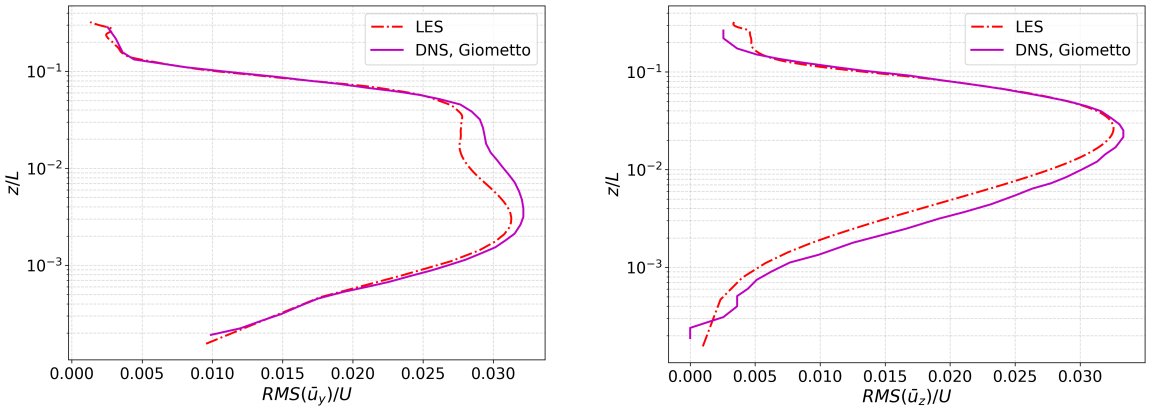


(a) Spanwise velocity fluctuations

(b) Vertical velocity fluctuations

Figure 2.4: Comparison of RMS values of $\overline{u}_y$ and $\overline{u}_z$ from the present $\alpha_{30}$ and the reference DNS data.

### 2.3.2 Analysis of Slope Angle Effects

The Large Eddy Simulation results for the three slope angles reveal the fundamental flow characteristics of anabatic boundary layers. All quantities are normalized using the characteristic parameters defined in Section 2.1.1, with vertical profiles presented on logarithmic scales to emphasize the different flow regions.

#### Mean Flow Structure

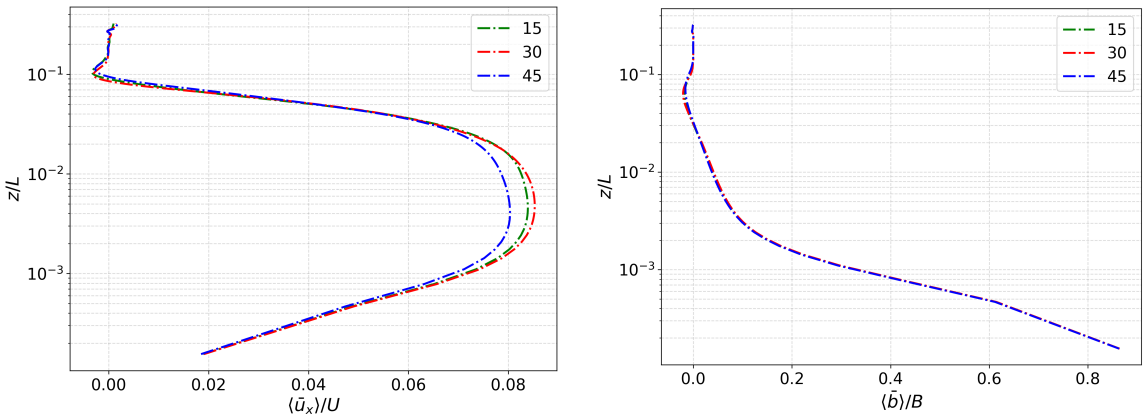


(a) Vertical profile of normalized mean streamwise velocity

(b) Vertical profile of normalized mean buoyancy

Figure 2.5: Mean profiles of the fundamental quantities

The mean streamwise velocity profiles (Figure 2.5a) demonstrate the classical anabatic flow structure across all three slope angles. The near-wall acceleration region ($z/L < 10^{-3}$) shows velocity increase due to positive buoyancy forcing, followed by a fully developed region ($10^{-3} < z/L < 10^{-1}$) containing the velocity maximum, and an outer decay region ($z/L > 10^{-1}$) where velocity approaches zero.
The mean buoyancy profiles (Figure 2.5b) confirm the three-layer structure characteristic of stratified flows ([Pope, 2000]): a high-gradient near-wall region, an intermediate region with local minimum corresponding to maximum turbulent activity, and an outer layer returning to neutral stratification. The negative values observed at $z/L \approx 10^{-1}$ in both velocity and buoyancy fields represent the back-flow region, arising from mass conservation requirements within the confined domain. A closer inspection of the velocity profiles reveals a consistent, albeit modest, reduction in the maximum streamwise velocity for the $\alpha = 45°$ case compared to the shallower slopes. This observed trend is physically consistent with the expected dynamics: on steeper slopes, a larger component of the buoyancy force acts to pull the fluid parcel directly away from the surface (in the wall-normal direction, $\hat{z}$), rather than accelerating it along the slope (in the streamwise direction, $\hat{x}$). Consequently, for a fixed surface buoyancy $b_S$, the effective acceleration driving the upslope flow is reduced as the slope angle $\alpha$ increases, leading to a lower peak velocity

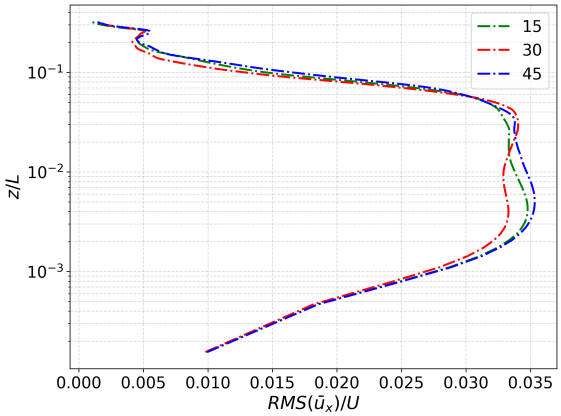


(a) Streamwise velocity fluctuations

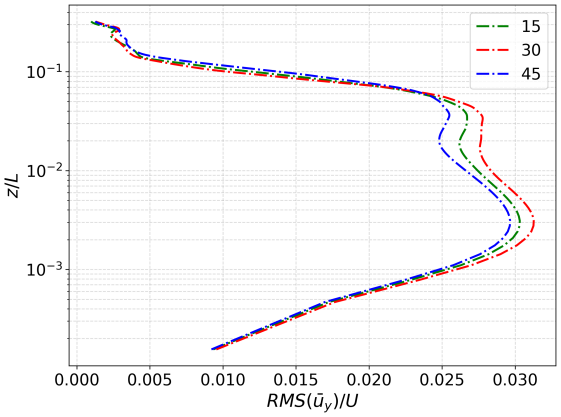


(b) Spanwise velocity fluctuations

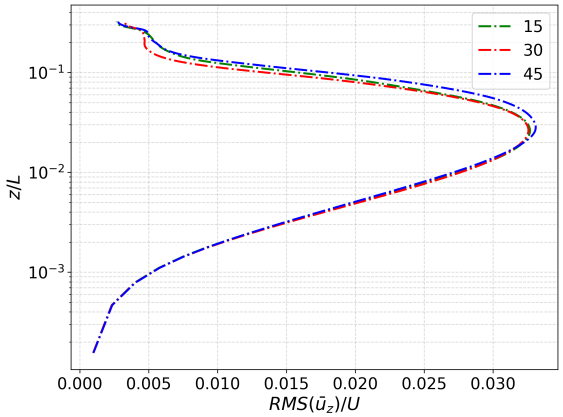


(c) Vertical velocity fluctuations

Figure 2.6: Vertical profiles of the velocity component standard deviations (RMS).

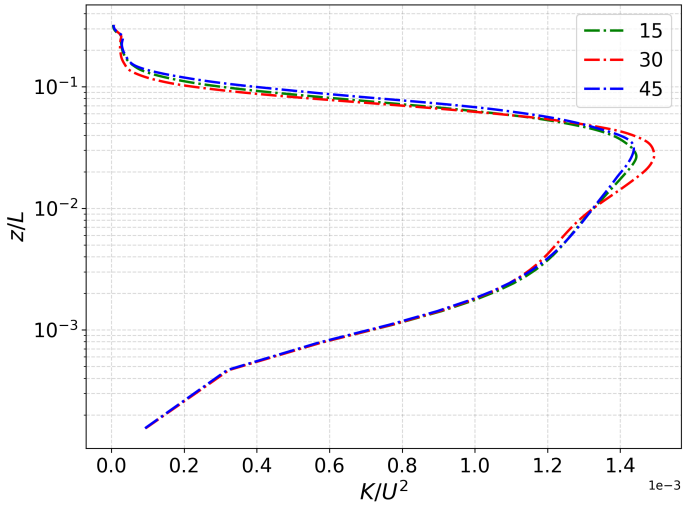


Figure 2.7: Vertical profile of normalized turbulent kinetic energy

The velocity fluctuation profiles (Figures 2.6a-2.6c) exhibit typical boundary layer anisotropy, with horizontal components exceeding vertical fluctuations, particularly near the wall. The turbulent kinetic energy distribution (Figure 2.7) peaks in the

intermediate region ($10^{-2} < z/L < 10^{-1}$), indicating maximum turbulence production through combined shear and buoyancy effects.

### Turbulent Transport Mechanisms

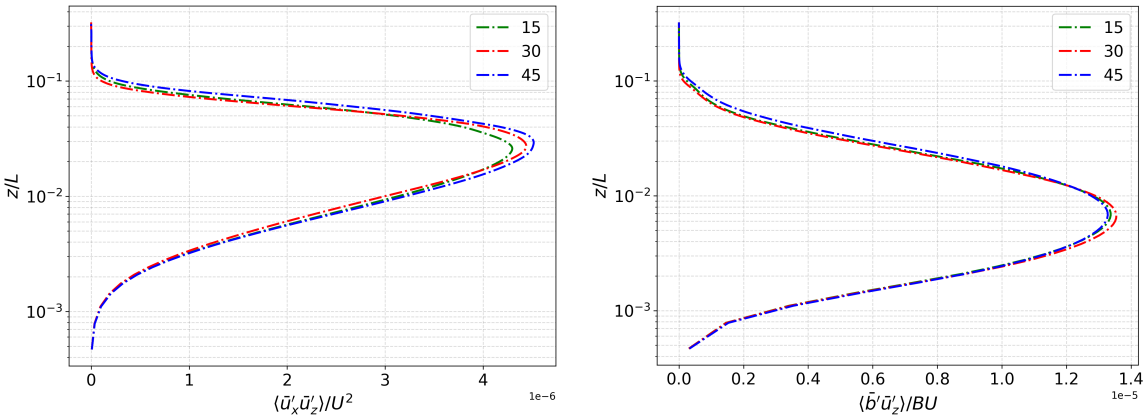


(a) Vertical turbulent momentum flux (b) Vertical turbulent buoyancy flux

Figure 2.8: Vertical profiles of the turbulent fluxes.

The turbulent momentum flux (Figure 2.8a) maintains positive values throughout the boundary layer, confirming net upward momentum transport characteristic of anabatic flows. Similarly, the turbulent buoyancy flux (Figure 2.8b) shows positive values across the domain, validating the gradient-diffusion hypothesis:

$$\langle \bar{b}' \bar{u}'_z \rangle = -\Gamma_T \frac{\partial \langle \bar{b} \rangle}{\partial z} \tag{2.12}$$

Given that the mean buoyancy gradient $\partial \langle \bar{b} \rangle / \partial z$ is negative while the flux $\langle \bar{b}' \bar{u}'_z \rangle$ is positive, this confirms downgradient transport with positive turbulent diffusivity $\Gamma_T > 0$.

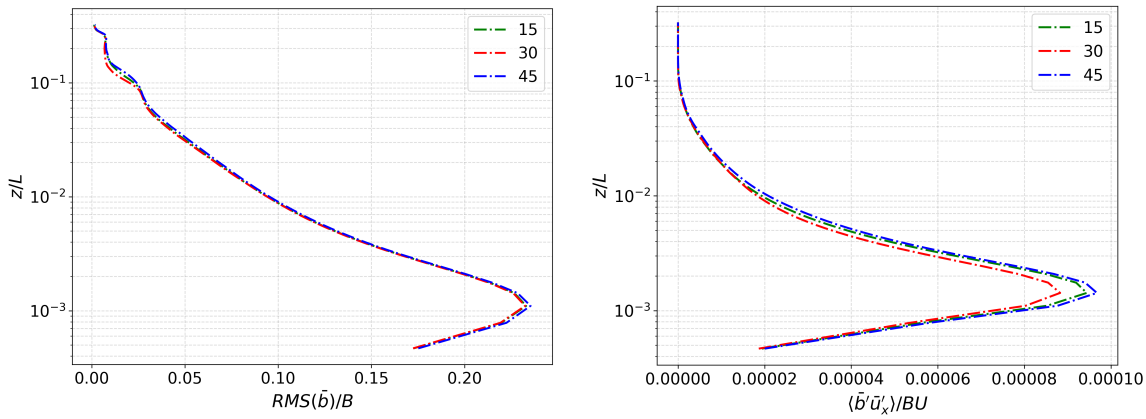


(a) Buoyancy fluctuations (b) Horizontal turbulent buoyancy flux

Figure 2.9: Profiles of buoyancy fluctuations and horizontal turbulent flux

The buoyancy fluctuations (Figure 2.9a) peak in the near-wall region where the mean buoyancy gradient is steepest, decreasing with height as the mean gradient weakens. The horizontal turbulent buoyancy flux (Figure 2.9b) shows significant values only in the near-wall region.

### 2.3.3 Instantaneous Flow Field Analysis

The analysis of instantaneous flow fields from the LES reveals the three-dimensional turbulent structures characteristic of anabatic flows. Unlike the time-averaged statistics presented previously, these fields capture the dynamic and intermittent nature of convective transport processes.

#### Vortical Structures and Thermal Plumes

The instantaneous vorticity field (Figure 2.10) reveals organized rotational structures that develop from surface heating. These structures manifest as thermal plumes - coherent columns of buoyant fluid rising from the heated surface and transporting heat and momentum vertically through the boundary layer. The plumes exhibit signifi-

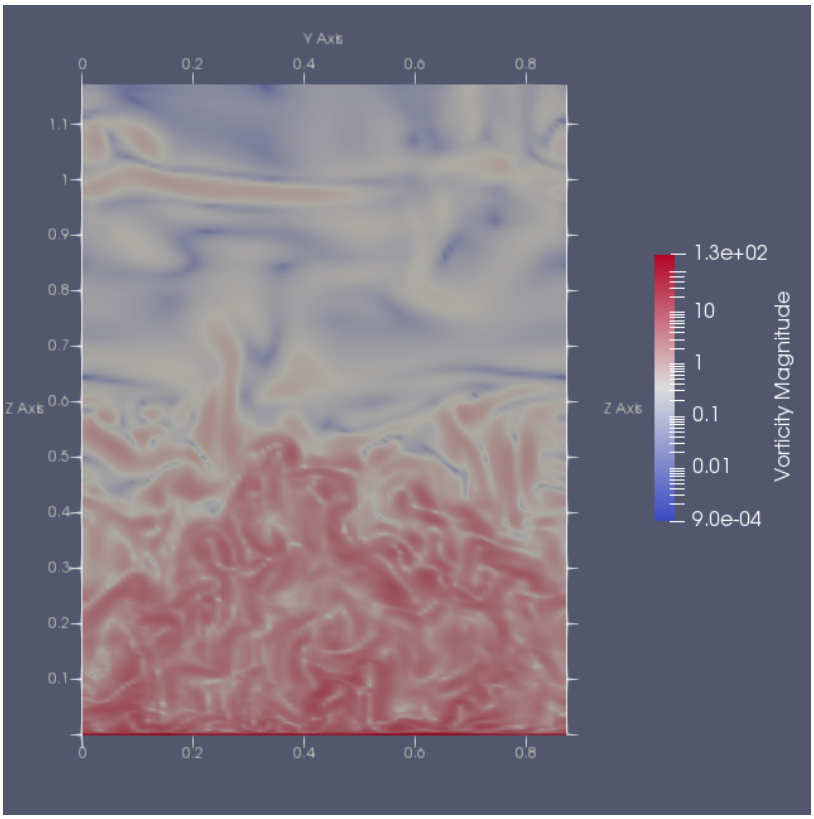


Figure 2.10: Vertical section showing instantaneous vorticity field

cant deformation from perfect vertical alignment due to interactions with the mean shear flow and neighboring turbulent structures. Vorticity generation occurs primarily through baroclinic production, where misaligned density and pressure gradients create fluid rotation according to:

$$\frac{D\boldsymbol{\omega}}{Dt} = \frac{1}{\rho^2}\nabla\rho \times \nabla p + \text{viscous terms} \tag{2.13}$$

where $\boldsymbol{\omega}$ is the vorticity vector representing local fluid rotation, $\rho$ is the fluid density varying with temperature, and $p$ is the pressure field. The cross product $\nabla\rho \times \nabla p$ generates vorticity when density gradients (from heating) are not parallel to pressure gradients, causing fluid elements to spin.

### Surface Flow Characteristics and Near-Wall Dynamics

The surface flow analysis reveals the fundamental mechanisms driving anabatic circulation. Figure 2.12 presents multiple aspects of the surface flow dynamics through different field variables that illuminate near-wall convective processes. The vertical

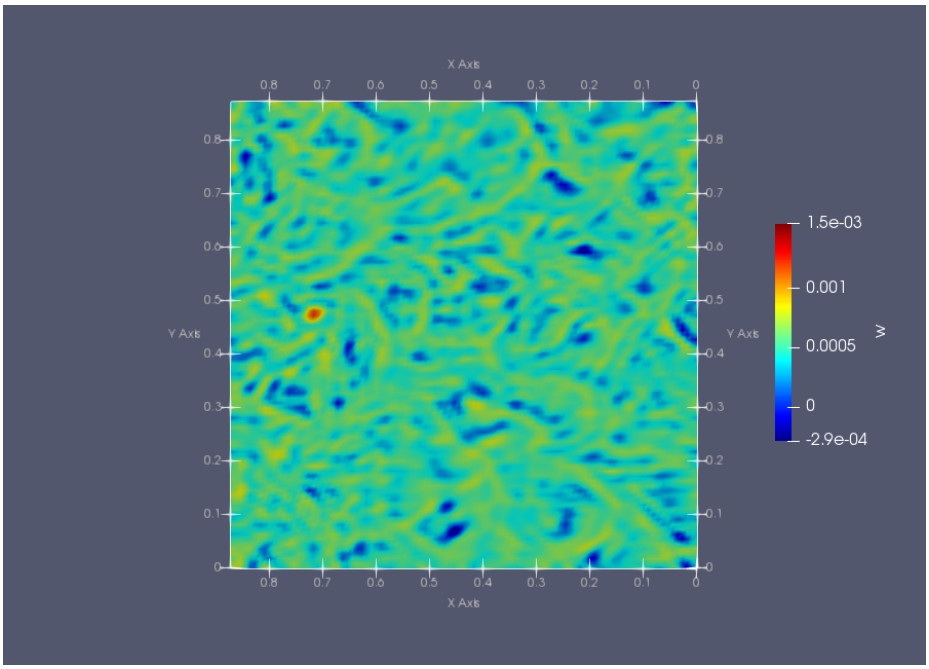


(a) Vertical velocity field $w$ at the surface

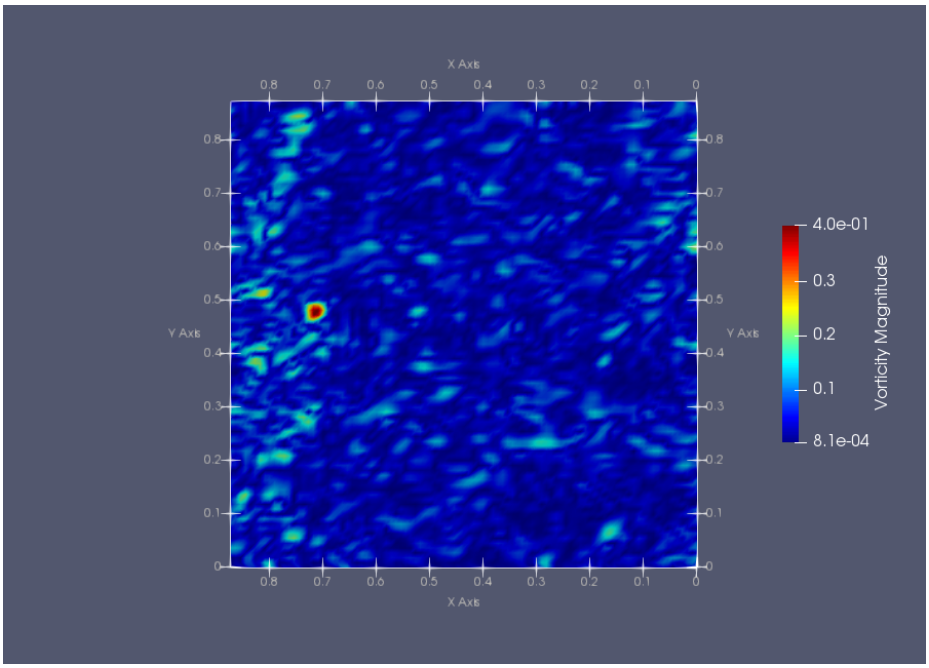


(b) Vorticity field at the surface

Figure 2.11: Vertical velocity $w$ and Vorticity at the surface

velocity field at the surface (Figure 2.11a) demonstrates discrete nucleation points where thermal plumes originate. Regions of positive vertical velocity (red) indicate plume initiation sites where buoyancy forces overcome viscous constraints imposed by the no-slip condition. The patchy distribution reflects the inherent instability of the heated boundary layer, where small perturbations amplify through buoyancy feed-

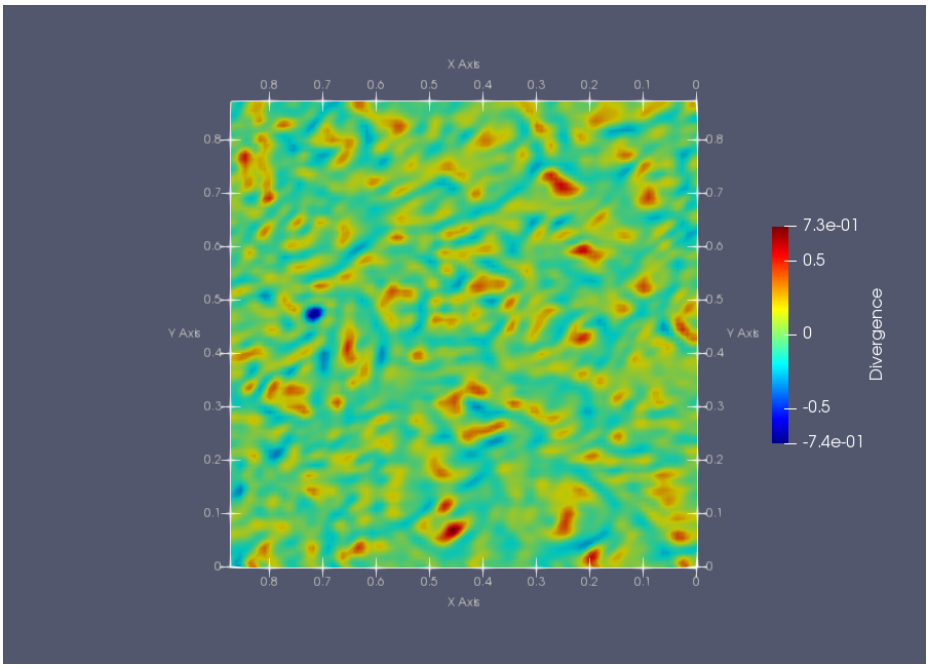


(a) $U$ divergence field at the surface

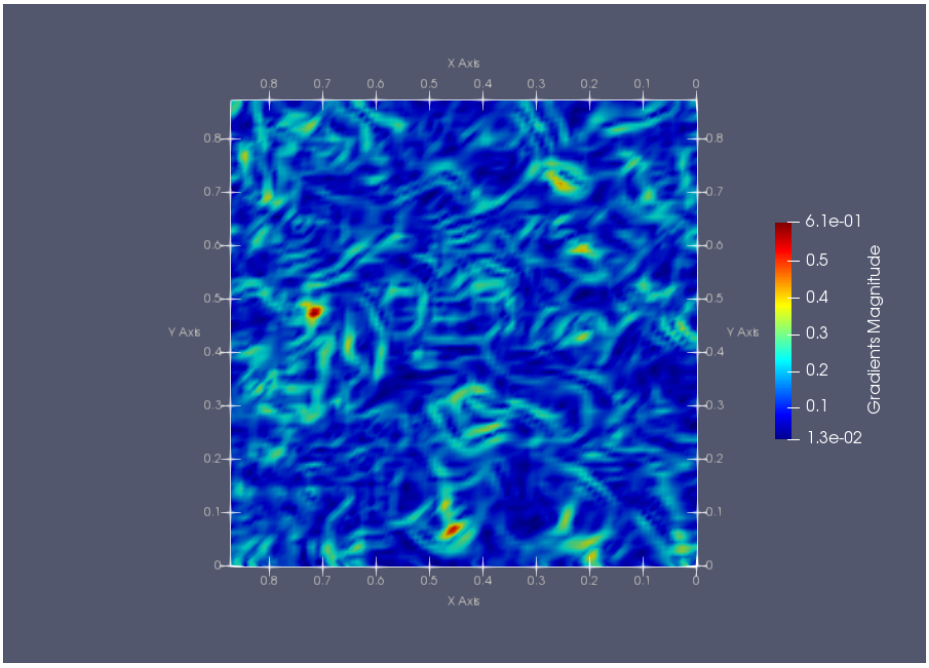


(b) $U$ gradient field at the surface

Figure 2.12: Flow field of $U$ at the surface ($z/L = 0$).

back.
The surface vorticity field (Figure 2.11b) reveals rotational dynamics associated with flow separation and thermal plume formation. High vorticity regions coincide with strong velocity gradients where upward-moving fluid creates shear with adjacent flow regions.
The velocity divergence field (Figure 2.12a) illustrates flow expansion patterns. The divergence $\nabla \cdot \mathbf{u}$ measures the rate of volumetric expansion of fluid elements - positive values indicate regions where heated fluid accelerates away from the surface, while negative values show convergence zones where cooler fluid flows toward thermal instability sites.

### Boundary Layer Development and Thermal Structure

At elevated positions within the boundary layer ($z/L = 0.15$), the flow transitions from immediate surface influence into regions where thermal plumes establish their characteristic structure (Figure 2.13). The vertical velocity field (Figure 2.13a) shows the organization of thermal plumes into more coherent structures. During ascent, plumes entrain ambient fluid through turbulent mixing, progressively diluting their thermal anomaly while increasing their mass flux and momentum transport capacity. The buoyancy gradient field (Figure 2.13b) identifies interfaces between ascending warm fluid and ambient air. The gradient magnitude $|\nabla b|$ quantifies the strength of density variations - large gradients mark plume boundaries where molecular diffusion and turbulent transport compete to homogenize the thermal field.

### Three-Dimensional Thermal Structure Analysis

The vertical velocity distribution on a constant buoyancy isosurface (Figure 2.14) provides insight into the complex three-dimensional geometry of thermal plumes. The isosurface topology reveals that plumes are not simple cylindrical structures but exhibit complex morphologies with branching, merging, and splitting behaviors. The irregular surface geometry reflects nonlinear dynamics governing plume evolution, where individual rising elements interact through pressure perturbations, leading to mutual attraction or repulsion depending on their relative phase and separation distance.

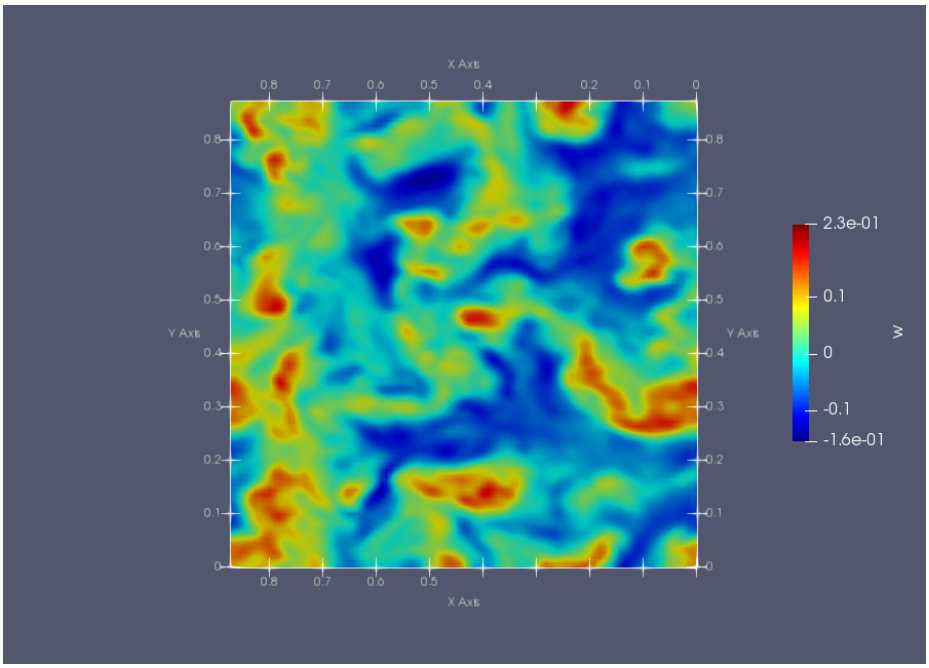


(a) Vertical velocity field $w$ at $z/L = 0.15$

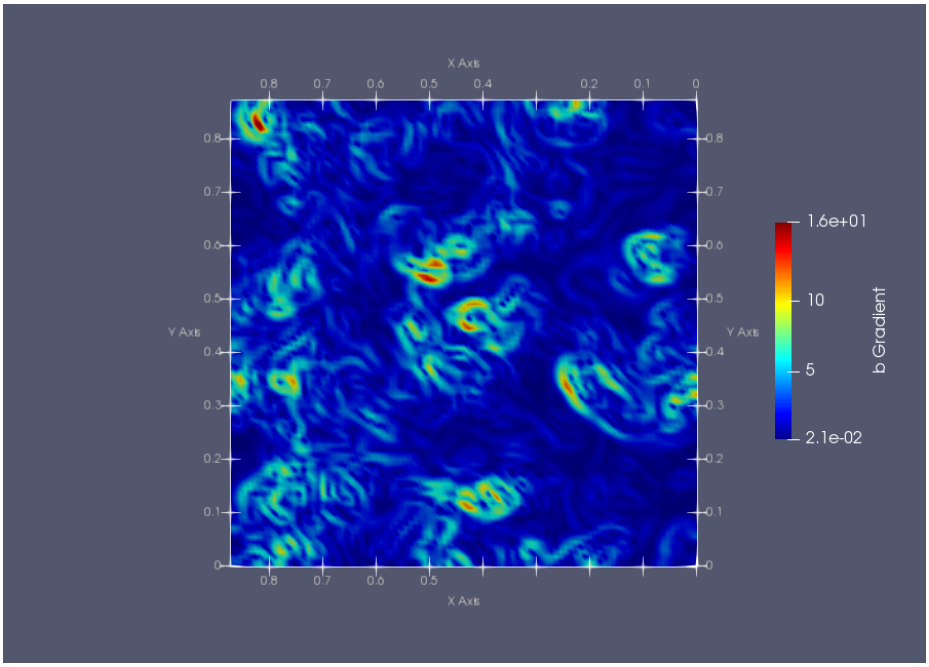


(b) Buoyancy gradient field at $z/L = 0.15$

Figure 2.13: Fluid dynamic fields in the boundary layer ($z/L = 0.15$).

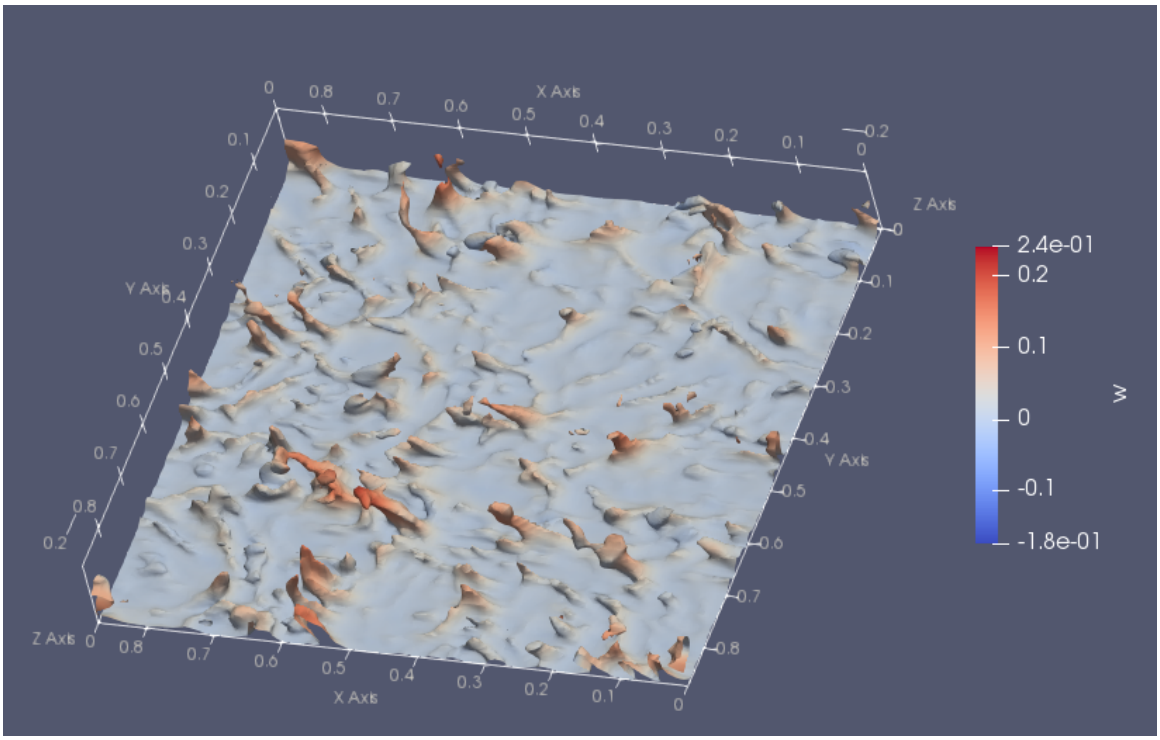


Figure 2.14: Vertical velocity field $w$ at the $b = 0.1b_{max}$ isosurface

### 2.3.4 Critical Analysis of Slope Angle Sensitivity

The most striking outcome of this parametric study is the unanticipated insensitivity of the flow statistics to changes in slope inclination. This result presents a significant divergence from the foundational work of [Prandtl et al., 2013] and the high-fidelity DNS data of [Giometto et al., 2017], both of which establish a clear dependence of anabatic flow structure on the slope angle.
Quantitative analysis reveals that the differences in mean velocity, buoyancy, turbulent kinetic energy, and flux profiles between the $\alpha = 15°$, $30°$, and $45°$ cases are negligible and fall within the margin of statistical uncertainty inherent to the LES approach. This suggests that the present computational framework, while successfully capturing the global characteristics of anabatic flow, fails to resolve the specific physical mechanisms through which topography modulates these dynamics.
Two principal constraints of the current methodology are hypothesized to be responsible for this limitation:

1. **Inherent Deficiencies of the SGS Closure:** The standard Smagorinsky model is notoriously dissipative and isotropic. Its tendency to overdamp turbulent fluctuations likely suppresses the smaller-scale, energy-containing eddies that are most responsive to changes in the orientation of the buoyancy force relative to the slope. This excessive damping effectively filters out the nuanced dynamics that differentiate steeper from shallower slopes, homogenizing the simulated flow fields.

2. **Computational and Parametric Constraints:** The selected Grashof number ($Gr = 2.1 \times 10^{11}$), while substantial, may not be sufficiently high to force the flow into a fully turbulent regime where inertial effects decisively dominate viscous constraints across all scales. In this transitional state, the flow's response to topographic forcing might be muted. Furthermore, the possibility of

numerical artifacts or insufficient statistical convergence for the extreme angles ($\alpha = 15°$, $45°$) cannot be entirely discounted, as their unique flow structures may require longer simulation times to achieve true stationarity.

Consequently, the immediate priority for future work must be to recompute the $\alpha = 15°$ and $\alpha = 45°$ cases with extended temporal averaging and stringent convergence monitoring. This will serve to conclusively eliminate inadequate sampling as a potential cause. Should the lack of sensitivity persist, it will robustly indict the SGS model's limitations.

# Chapter 3

# Conclusions

This thesis has detailed the implementation and results of a Large-Eddy Simulation study designed to investigate the influence of slope angle on anabatic flow dynamics. A numerical framework was established within OpenFOAM, incorporating a rotated coordinate system and critical solver modifications to accurately represent the physics of a stratified flow on an infinite inclined plane with cyclic boundaries.
The simulation successfully reproduced the canonical features of anabatic flows. The instantaneous flow fields revealed the formation and evolution of coherent structures, such as thermal plumes and longitudinal vortices, which are the hallmark of convective boundary layers driven by surface heating. The validation of the $\alpha = 30°$ case against the DNS benchmark of [Giometto et al., 2017] demonstrated excellent agreement for both first and second-order statistics, confirming the model's capability to capture the mean flow structure and turbulent quantities for a specific configuration. However, the central finding of this study is the surprising absence of a clear sensitivity to slope inclination. The comparative analysis showed that the statistical properties of the flow were virtually identical for angles of 15°, 30°, and 45°. This lack of dependence is unexpected, not in agreement with theoretical and high-fidelity numerical evidence. A few hypotheses are formulated to explain this result: the excessive dissipation inherent in the standard Smagorinsky model, which likely suppresses the scale-specific turbulent interactions crucial for topographic modulation, the potential influence of the selected Grashof number and, possiby, of numerical issues in the simulations of the extreme angles, requiring verification through recomputation, are also acknowledged as contributing factors.
Based on these considerations, an additional work is needed, specifically exploring the following points:

1. **Verification and Validation:** The paramount next step is to re-run the $\alpha = 15°$ and $\alpha = 45°$ simulations to ensure statistical robustness and rule out numerical artifacts, thereby confirming the result's validity.

2. **Advanced Turbulence Modeling:** Subsequent studies should employ advanced SGS closures, such as Dynamic or Anisotropic Minimum Dissipation models, to mitigate excessive dissipation and better capture the physics of stratified flows over complex topography.

3. **Extended Parameter Study:** Exploring a higher Grashof number regime would help bridge the gap towards more realistic atmospheric conditions and potentially amplify turbulent scaling effects.

In summary, this work provides a validated LES framework for simulating anabatic flows and successfully captures their characteristic coherent structures. Yet, it also exposes a possible vulnerability of standard subgrid-scale models in simulating topographically-sensitive turbulence. It underscores the necessity of meticulous model selection and paves the way for more sophisticated numerical experiments to truly elucidate the role of slope angle in governing anabatic wind systems.

# Bibliography

[Alba et al., 2000] Alba, F., De La Guardia, C. D., and Comtois, P. (2000). The effect of meteorological parameters on diurnal patterns of airborne olive pollen concentration. *Grana*, 39(4):200–208.

[Cintolesi et al., 2021] Cintolesi, C., Di Santo, D., Barbano, F., and Di Sabatino, S. (2021). Anabatic flow along a uniformly heated slope studied through large-eddy simulation. *Atmosphere*, 12(7):850.

[Drake and Farrow, 1988] Drake, V. A. and Farrow, R. A. (1988). The influence of atmospheric structure and motions on insect migration. *Annual Review of Entomology*, 33(1):183–210.

[Fedorovich and Shapiro, 2009a] Fedorovich, E. and Shapiro, A. (2009a). Structure of numerically simulated katabatic and anabatic flows along steep slopes. *Acta Geophysica*, 57(4):981–1010.

[Fedorovich and Shapiro, 2009b] Fedorovich, E. and Shapiro, A. (2009b). Turbulence and waves in numerically simulated slope flows. *Mechanics 38; Industry*, 10(3–4):175–179.

[Feigenwinter et al., 2010] Feigenwinter, C., Montagnani, L., and Aubinet, M. (2010). Plot-scale vertical and horizontal transport of $CO_2$ modified by a persistent slope wind system in and above an alpine forest. *Agricultural and Forest Meteorology*, 150(5):665–673. Special Issue on Advection: ADVEX and Other Direct Advection Measurement Campaigns.

[Giometto et al., 2017] Giometto, M. G., Katul, G. G., Fang, J., and Parlange, M. B. (2017). Direct numerical simulation of turbulent slope flows up to Grashof number $gr = 2.1 \times 10^{11}$. *Journal of Fluid Mechanics*, 829:589–620.

[Griffiths et al., 2014] Griffiths, A. D., Conen, F., Weingartner, E., Zimmermann, L., Chambers, S. D., Williams, A. G., and Steinbacher, M. (2014). Surface-to-mountaintop transport characterised by radon observations at the jungfraujoch. *Atmospheric Chemistry and Physics*, 14:12763–12779.

[Hilel Goldshmid et al., 2018] Hilel Goldshmid, R., Bardoel, S. L., Hocut, C. M., Zhong, Q., Liberzon, D., and Fernando, H. J. S. (2018). Separation of upslope flow over a plateau. *Atmosphere*, 9(5):165.

[Hunt et al., 2003] Hunt, J. C. R., Fernando, H. J. S., and Princevac, M. (2003). Unsteady thermally driven flows on gentle slopes. *Journal of the Atmospheric Sciences*, 60(17):2169–2182.

[Kundu et al., 2012] Kundu, P., Cohen, I., and Dowling, D. (2012). *Fluid Mechanics*. Science Direct e-books. Elsevier Science.

[McNider, 1982] McNider, R. T. (1982). A note on velocity fluctuations in drainage flows. *Journal of Atmospheric Sciences*, 39(7):1658 – 1660.

[Mezgec et al., 2017] Mezgec, K., Stenni, B., Crosta, X., Masson-Delmotte, V., Baroni, C., Braida, M., Ciardini, V., Colizza, E., Melis, R., Salvatore, M. C., et al. (2017). Holocene sea ice variability driven by wind and polynya efficiency in the Ross Sea. *Nature Communications*, 8(1):1334.

[Pope, 2000] Pope, S. (2000). *Turbulent Flows*. Cambridge University Press.

[Prandtl et al., 2013] Prandtl, L., Oswatitsch, K., and Wieghardt, K. (2013). *Führer durch die Strömungslehre*. Springer, Berlin, Heidelberg.

[Princevac and Fernando, 2007] Princevac, M. and Fernando, H. J. S. (2007). A criterion for the generation of turbulent anabatic flows. *Physics of Fluids*, 19(10):105102.

[Reuten et al., 2007] Reuten, C., Steyn, D. G., and Allen, S. E. (2007). Water tank studies of atmospheric boundary layer structure and air pollution transport in upslope flow systems. *Journal of Geophysical Research: Atmospheres*, 112(D11):D11312.

[Sabatier et al., 2020] Sabatier, T., Largeron, Y., Paci, A., Lac, C., Rodier, Q., Canut, G., and Masson, V. (2020). Semi-idealized simulations of wintertime flows and pollutant transport in an Alpine valley. Part II: Passive tracer tracking. *Quarterly Journal of the Royal Meteorological Society*, 146(727):827–845.

[Schumann, 1990] Schumann, U. (1990). Large-eddy simulation of the upslope boundary layer. *Quarterly Journal of the Royal Meteorological Society*, 116(493):637–670.

[Sharples, 2009] Sharples, J. J. (2009). An overview of mountain meteorological effects relevant to fire behaviour and bushfire risk. *International Journal of Wildland Fire*, 18(7):737–754.

[Whiteman, 2000] Whiteman, C. (2000). *Mountain Meteorology: Fundamentals and Applications*. Oxford University Press.

[Whiteman, 1982] Whiteman, C. D. (1982). Breakup of temperature inversions in deep mountain valleys: Part i. observations. *Journal of Applied Meteorology and Climatology*, 21(3):270–289.

[Xiao and Senocak, 2020] Xiao, C.-N. and Senocak, I. (2020). Stability of the anabatic Prandtl slope flow in a stably stratified medium. *Journal of Fluid Mechanics*, 885:A13.